RESEARCH ARTICLE

Defect engineering of ternary Cu–In–Se quantum dots for boosting photoelectrochemical hydrogen generation

Shi Li[1] | Sung-Mok Jung[2] | Wookjin Chung[1] | Joo-Won Seo[2] | Hwapyong Kim[1] (ORCID) | Soo Ik Park[1] | Hyo Cheol Lee[1] | Ji Su Han[1] | Seung Beom Ha[2] | In Young Kim[3] | Su-Il In[1,4] | Jae-Yup Kim[2] | Jiwoong Yang[1,4] (ORCID)

[1]Department of Energy Science and Engineering, Daegu Gyeongbuk Institute of Science and Technology (DGIST), Daegu, Republic of Korea

[2]Department of Chemical Engineering, Dankook University, Yongin, Republic of Korea

[3]Department of Chemistry and Nanoscience, College of Natural Science, Ewha Womans University, Seoul, Republic of Korea

[4]Energy Science and Engineering Research Center, Daegu Gyeongbuk Institute of Science and Technology (DGIST), Daegu, Republic of Korea

Correspondence

Su-Il In and Jiwoong Yang, Department of Energy Science and Engineering, Daegu Gyeongbuk Institute of Science and Technology (DGIST), Daegu 42988, Republic of Korea.
Email: insuil@dgist.ac.kr and jiwoongyang@dgist.ac.kr

Jae-Yup Kim, Department of Chemical Engineering, Dankook University, Yongin 16890, Republic of Korea.
Email: jykim@dankook.ac.kr

Abstract

Heavy-metal-free ternary Cu–In–Se quantum dots (CISe QDs) are promising for solar fuel production because of their low toxicity, tunable band gap, and high light absorption coefficient. Although defects significantly affect the photophysical properties of QDs, the influence on photoelectrochemical hydrogen production is not well understood. Herein, we present the defect engineering of CISe QDs for efficient solar-energy conversion. Lewis acid–base reactions between metal halide–oleylamine complexes and oleylammonium selenocarbamate are modulated to achieve CISe QDs with the controlled amount of Cu vacancies without changing their morphology. Among them, CISe QDs with In/Cu = 1.55 show the most outstanding photoelectrochemical hydrogen generation with excellent photocurrent density of up to 10.7 mA cm^{-2} (at 0.6 V$_{RHE}$), attributed to the suitable electronic band structures and enhanced carrier concentrations/lifetimes of the QDs. The proposed method, which can effectively control the defects in heavy-metal-free ternary QDs, offers a deeper understanding of the effects of the defects and provides a practical approach to enhance photoelectrochemical hydrogen generation.

KEYWORDS

copper–indium–selenide, defect engineering, photoelectrochemical hydrogen generation, quantum dots, solar hydrogen

Shi Li and Sung-Mok Jung contributed equally to this study.

1 | INTRODUCTION

Photoelectrochemical (PEC) hydrogen production[1–6] is a simple, sustainable, environmentally friendly, and cost-effective way to produce clean hydrogen.[7–14] Conventionally, metal-oxide semiconductors, including TiO_2, $BiVO_4$, and WO_3, have been extensively used as PEC photoelectrodes because of their appropriate electronic energy levels (i.e., higher conduction band position than the redox potential of H_2/H_2O (0 V_{NHE}), lower valence band position than that of O_2/H_2O (1.23 V_{NHE}), and high stability during water splitting.[15–18] However, these materials can only absorb light within a limited energy range because of their wide band gaps, which limits their overall solar-to-hydrogen efficiency. For example, TiO_2, a representative oxide semiconductor material used for solar-energy conversion, has a band gap of 3.2 eV.[18–20] This limits the light absorbed by this material to the ultraviolet region, which is approximately 4% of the overall sunlight. To overcome this limitation, a strategy for fabricating heterojunctions with absorbers with narrower band gaps was proposed.[21–24] The second absorber can produce additional charge carriers by absorbing longer wavelengths (i.e., visible and/or near-infrared light), which most oxide semiconductors cannot utilize. These photogenerated carriers are then transferred to the oxide semiconductors, leading to enhanced hydrogen generation.

Semiconductor quantum dots (QDs) have unique optical and electronic properties, such as tunable band gap and band alignment[4–6,25] and long carrier lifetime of hot electrons.[26] Therefore, QD sensitization of metal-oxide semiconductors is currently regarded as a promising method for effective PEC hydrogen generation.[4–6,25,27–32] To date, QD/metal-oxide junctions have been widely used for various applications, such as solar cells,[33,34] photodetectors,[35,36] and light-emitting diodes.[37,38] Despite the superior optical properties of semiconductor QDs, most of the previous studies have been performed using toxic Cd-chalcogenide[39] or Pb-chalcogenide QDs. As an alternative, heavy-metal-free I–III–VI QDs have recently emerged as promising candidates for solar-energy conversion because of their low toxicity, band gap enabling absorption up to the near-infrared range, and high light extinction coefficient.[40,41] Recently, researchers have begun applying these materials for PEC hydrogen production, demonstrating promising results. However, these initial studies focused on the fabrication process of QD photoanodes (e.g., core–shell structure,[42] metal doping,[43] morphology,[44] etc.) to explore the applicability of I–III–VI group QDs for PEC,[45–48] and extensive research is required to gain a fundamental understanding of the material design principles for efficient PEC hydrogen generation.

Defects in semiconductor materials significantly affect their electrical and photophysical properties, such as free carrier mobility and carrier lifetime.[49–52] Furthermore, this effect is even more complicated for semiconductors with multiple elements because they have various types of point-defect types. For example, intrinsic defects, including vacancies (V_{Cu}, V_{In}, and V_{Se}), interstitial defects (Cu_i, In_i, and Se_i), and anti-site defects (Cu_{In}, In_{Cu}, etc.), have been observed in Cu–In–Se (CISe) thin films (even without impurity atoms).[53,54] Therefore, the changes in stoichiometry in CISe thin films modify the type and density of intrinsic defects, determining the type of major carriers, carrier lifetime, and carrier concentrations.[53–55] The influence of the defects is stronger for smaller crystals because of their high surface-to-volume ratio and limited crystal size.[56,57] A recent study revealed that the photoluminescence of CISe QDs can be significantly varied, even with minor changes in the atomic configuration of the QDs,[58,59] emphasizing the importance of defect control. However, the effects of the defects in these CISe QDs on their photophysical properties, including the resulting PEC properties, are underexplored owing to the difficulties in controlling the defects during the synthesis of ternary semiconductor QDs. For example, the size of the nanocrystals affects the stoichiometry of CISe QDs; as the size of the QD decreases, the In/Cu molar ratio increases.[60,61] In other words, the composition of CISe QDs, which is one of the most effective ways of controlling defects in ternary semiconductor materials, cannot be independently controlled without affecting their size and shape.

Herein, we report tunable defect engineering of ternary Cu–In–Se (CISe) QDs for PEC hydrogen generation by regulating the reactivity of metal precursors in the QD synthesis process. The Lewis acid–base reactions between metal halide–oleylamine complexes and oleylammonium selenocarbamate were controlled by adjusting the relative strengths of the acids, producing CISe QDs with a wide range of In/Cu ratios without changing their size and shape. This enabled a detailed study of the effect of the defects on the optical and electrical properties of the QDs. The QDs were subsequently used as solar energy harvesters in QD-sensitized photoanodes, and the effects of defects on PEC hydrogen generation were systematically investigated. Furthermore, the performance of the QD-sensitized solar cells (QDSCs) was optimized by modifying the QD composition, and the mechanisms underlying the enhanced performance of the solar-energy conversion systems using the QDs were clarified. Our results demonstrate a simple and effective way to control the defects in eco-friendly ternary QDs

and highlight their potential as an alternative for toxic conventional QDs in high-efficiency solar-energy conversion.

2 | EXPERIMENTAL SECTION

2.1 | Materials

Copper (I) chloride (99.999%), copper (I) bromide (99.998%), copper (I) iodide (99.998%), indium (III) chloride (99.999%), indium (III) bromide (99.99%), and indium (III) iodide (99.999%) were purchased from Alfa Aesar. Dichloromethane (99.8%), oleylamine (OAm, technical grade), oleic acid (OA, technical grade), trioctylphosphine (TOP, 97%), selenium (Se) powder (99.99%), titanium diisopropoxide bis (acetylacetonate) (75 wt%), tetraethyl orthosilicate (98%), $Zn(NO_3)_2 \cdot 6H_2O$ (98%), and sodium sulfide (Na_2S) were purchased from Sigma-Aldrich. Anhydrous ethanol (EtOH), butanol (BuOH, 99%), acetonitrile (99.5%), and sodium sulfite (Na_2SO_3, 97.0%, anhydrous) were purchased from Samchun Chemicals. NH_4OH (25% solution) was purchased from Daejung Chemicals & Metals. The OAm was dried under vacuum for 2 h before use. Carbon monoxide (CO) gas was purchased from Sumitomo Seika Chemical Co.

2.2 | Synthesis of defect-engineered CISe QDs

Defect-engineered CISe QDs were synthesized through the Lewis acid–base reactions between metal halide–OAm complexes and oleylammonium selenocarbamate. A metal halide–OAm complex[62] solution was prepared by heating the metal halide precursors in OAm under vacuum (120°C, 30 min). The final cation precursor solution contained 0.5 mmol of CuX–OAm complexes and 0.5 mmol of InX_3–OAm complexes in 15.0 mL of OAm (X = Cl⁻, Br⁻, or I⁻). To control the In/Cu ratio of the final QDs, various combinations of metal halide–OAm complex solutions were used. For example, the combinations of CuI–OAm/$InCl_3$–OAm, CuI–OAm/$InBr_3$–OAm, CuI–OAm/InI_3–OAm, CuBr–OAm/InI_3–OAm, and CuCl–OAm/InI_3–OAm were used for the synthesis of CISe 1, 2, 3, 4, and 5, respectively. The Se precursor solution was prepared by reacting 5.0 mmol of Se powder in 10.0 mL of OAm with CO gas at 80°C for 1 h, producing oleylammonium selenocarbamate.[63] 1.0 mmol of oleylammonium selenocarbamate was rapidly injected into the metal halide–OAm solution at 70°C. The reacting mixture was heated to 190°C (heating rate: 15°C min⁻¹) and was

kept at this temperature for 20 min. The CISe QDs produced were precipitated by the standard centrifugation with excess anhydrous ethanol (total two cycles). For the first cycle of the centrifugation, a drop of TOP was added to anhydrous ethanol to remove any residual Se precursor. The resulting products were used for further applications or characterization, either in powder form or as a solution dispersed in dichloromethane.

2.3 | Preparation and characterization of photoanodes using CISe QDs

Photoanodes were prepared using modified methods from our previous work on CISe QDSCs.[60,64] Typically, fluorine-doped tin oxide (FTO) glass (TEC-A7; Pilkington) was cleaned by sonification (25 min for acetone and ethanol) and UV/O_3 treatment (20 min). For the coating of a dense TiO_2 thin layer onto the FTO glass, 7.5 wt% solution of titanium diisopropoxide-bis(acetylacetonate) in *n*-butanol was spin-cast, followed by annealing in air (475°C, 15 min). A commercial TiO_2 paste (Ti-Nanoxide T/SP; Solaronix) was further coated using the doctor blade technique and subsequently annealed in air (525°C, 35 min). For sensitization with CISe QDs, the annealed TiO_2 film on the FTO glass was soaked in a solution of colloidal CISe QDs dispersed in dichloromethane for 6 h. The CISe QDs/TiO_2 film was then washed with dichloromethane and dried under a nitrogen (N_2) gas flow. For surface passivation, the surface of the CISe QDs/TiO_2 film was coated with zinc sulfide (ZnS) using a conventional successive ionic layer adsorption and reaction method (three cycles), providing inorganic passivation layers for enhanced stability with the suppressed surface charge recombination. The CISe QDs/TiO_2 film was alternatively dipped in a 0.05 M ethanolic solution of $Zn(NO_3)_2 \cdot 6H_2O$ and a 0.05 M solution of Na_2S in deionized water/methanol (1:1, v/v) for 1 min each. Additional SiO_2 passivation layers were deposited by chemical bath deposition (CBD) according to a previously reported procedure for QDSCs.[65] The ZnS-coated CISe QDs/TiO_2 film was immersed in an ethanolic solution containing 0.01 M tetraethyl orthosilicate and 0.1 M NH_4OH for 70 min, followed by washing with deionized water and drying in air.

The PEC performance was evaluated in a quartz cell with a three-electrode system using a potentiostat (Multi Autolab M204; Metrohm). The CISe QDs/TiO_2 film, Pt mesh, and mercury/mercury oxide (Hg/HgO) electrodes were used as the working, counter, and reference electrodes, respectively. The electrolyte for the PEC measurement was composed of 0.25 M sodium sulfide (Na_2S) and 0.35 M sodium sulfite (Na_2SO_3) in deionized water (pH ~12.8). For

the experiments without sacrificial agents, a 0.5 M Na_2SO_4 aqueous solution (pH ~6.0) was used. The active area of each cell (0.25 ± 0.03 cm^2) was measured using a CCD camera (Moticam 1000). The hydrogen evolution was determined under one-sun illumination (100 mW cm^{-2}) using a 100-W xenon lamp (LCS-100; Oriel) with an AM 1.5 G filter. A potentiostat (VSP; Bio-Logic) was used to apply an external bias to the PEC system during chronoamperometry tests. The evolved hydrogen was analyzed by gas chromatography (GC) (7890 B; Agilent) using a packed MoleSieve 5A column (6 ft. length and 2.1 mm inner diameter). Further experimental details are provided in the Supporting Methods.

3 | RESULTS AND DISCUSSION

3.1 | Synthesis of CISe QDs with controlled In/Cu ratios

CISe QDs with a tunable In/Cu ratio were synthesized using a facile hot-injection method by controlling the Lewis acid–base reactions between metal halide–oleylamine complexes and oleylammonium selenocarbamate (Figure 1A and Section 2). Based on the Lewis acid–base theory, oleylammonium selenocarbamate (Se precursor) is considered as a Lewis base, and reactive copper (I) halide (CuX)–oleylamine

(OAm) and indium (III) halide (InX$_3$)–OAm complexes are considered as Lewis acids. Changing the halide anion (X = Cl$^-$, Br$^-$, or I$^-$) results in different Lewis acidic strengths of metal halide–OAm complexes, resulting in different reactivities with Se precursors. The Lewis acidic strengths of CuX–OAm complexes are in the order of CuI > CuBr > CuCl, while the order for InX$_3$–OAm complexes is InI$_3$ > InBr$_3$ > InCl$_3$. The chemical composition of CISe QDs can be fine-tuned by adjusting the combinations of CuX and InX$_3$ using their relative Lewis acidic strengths to balance the reactivity between Cu$^+$ and In^{3+}, which is a key factor for achieving defect control in I–III–VI QDs.

Figure 1B–F shows the as-synthesized CISe QDs with different combinations of Cu and In precursors (labeled as CISe 1–5 with In/Cu molar ratios of 1.29, 1.33, 1.55, 1.60, and 1.83, respectively). The QDs are quasi-spherical, with a narrow size distribution (Figure S1). No noticeable changes in the morphology and size are observed for any of the combinations of precursors, which is beneficial for studying the effect of the composition on the structural and photophysical properties of QDs. The chemical composition of the QDs was determined using inductively coupled plasma optical emission spectroscopy. As shown in Figure S2A and Table 1, the CISe QDs were synthesized with a wide range of In/Cu molar ratios from 1.29 to 1.83. This indicates that the synthesis method is suitable for modulating the composition of QDs by
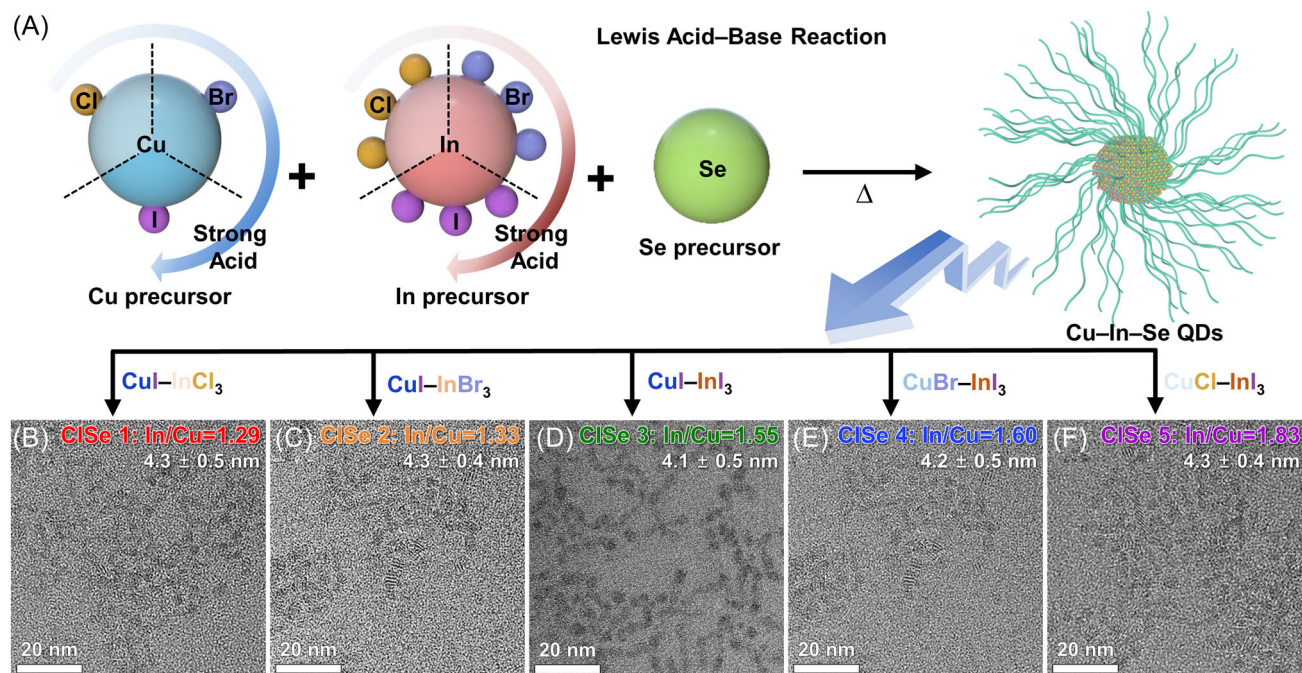
FIGURE 1 Synthesis of CISe QDs with controlled In/Cu ratios. (A) Schematic of the method for controlling Lewis acid–base reactions to synthesize CISe QDs with controlled In/Cu ratios. Oleylamine was omitted in the illustration for simplicity. (B–F) Transmission electron microscopy images of CISe QDs with various In/Cu molar ratios, labeled as CISe 1 (In/Cu = 1.29), CISe 2 (In/Cu = 1.33), CISe 3 (In/Cu = 1.55), CISe 4 (In/Cu = 1.60), and CISe 5 (In/Cu = 1.83).

TABLE 1 Synthesis of CISe QDs with controlled In/Cu ratios.

Samples	Cu–In precursor	In/Cu (ICP)[a]	Size (TEM) (nm)[b]
CISe 1	CuI–InCl$_3$	1.29 ± 0.03	4.3 ± 0.5
CISe 2	CuI–InBr$_3$	1.33 ± 0.03	4.3 ± 0.4
CISe 3	CuI–InI$_3$	1.55 ± 0.03	4.1 ± 0.5
CISe 4	CuBr–InI$_3$	1.60 ± 0.04	4.2 ± 0.5
CISe 5	CuCl–InI$_3$	1.83 ± 0.06	4.3 ± 0.4

Abbreviations: CISe, Cu–In–Se; QD, quantum dot; TEM, transmission electron microscopy.

[a]$n = 5$ (from five different reaction pots).

[b]$n = 200$ (from 200 QDs in TEM images) for the statistical data.

simply changing the metal precursors without corresponding changes in the QD size. We selected a series of 4-nm-diameter QDs as model materials for this study because of their excellent light absorption and ability to transfer charge to TiO$_2$, as demonstrated in previous studies on CISe QDSCs.[60,64]

3.2 | Structure characterization of CISe QDs

X-ray diffraction (XRD) analysis confirmed that all QDs had a tetragonal chalcopyrite CuInSe$_2$ crystal structure, regardless of the In/Cu molar ratio (Figure 2A). The
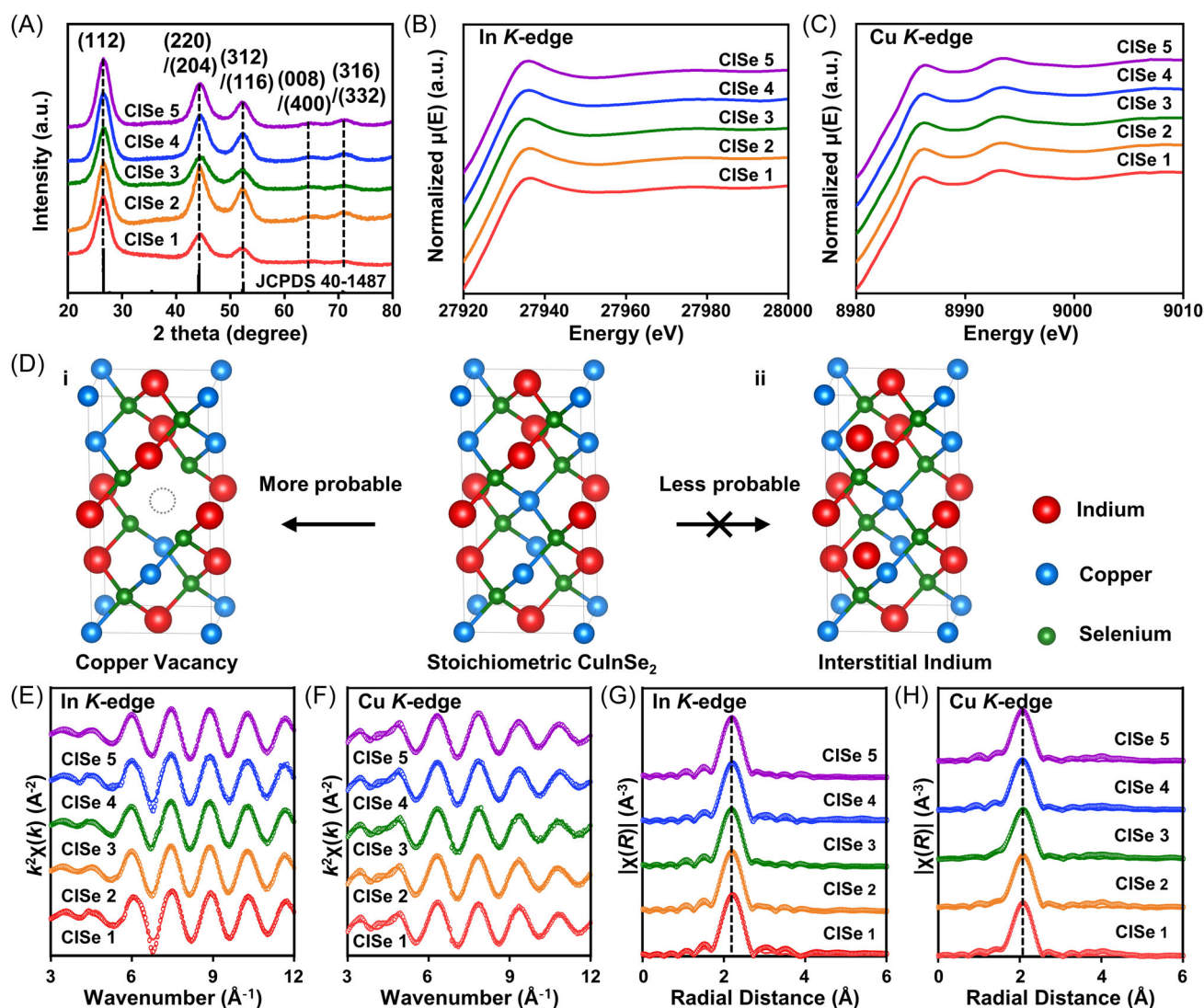
FIGURE 2 Structural characterization of CISe QDs. (A) XRD patterns, (B) In K-edge, and (C) Cu K-edge XANES spectra of CISe 1–5. (D) Two proposed crystal models for In-rich CISe QDs: (i) formation of Cu vacancies and (ii) formation of interstitial or anti-site In atoms. (E) In K-edge and (F) Cu K-edge k^2-weighted EXAFS oscillations of CISe 1–5. (G) In K-edge and (H) Cu K-edge FT spectra of CISe 1–5. Solid lines and circled patterns correspond to the fitted and experimental data.

positions of the main peaks in the XRD patterns are similar regardless of the composition (Table S1 and Figure S2), suggesting that changes in the In/Cu ratio do not change the basic crystal structure of QDs. Although the composition of CISe QDs is between that of α-CuInSe$_2$ and β-CuIn$_3$Se$_5$, the tetragonal distortion of the QDs is almost similar to that of α-CuInSe$_2$,[66] implying that the changes in the composition of the QDs are caused by defect formation rather than the formation of a different crystal phase. In addition, the binding energies of the Cu $2p_{3/2}$ and Cu $2p_{1/2}$ in X-ray photoelectron spectroscopy (XPS) spectra correspond to the Cu$^+$ oxidation state, while those of In $3d_{5/2}$ and In $3d_{3/2}$ correspond to the In^{3+} oxidation state (Figure S3). X-ray absorption near-edge structure (XANES) spectra show consistent results (Figure 2B,C). The findings indicate that the QDs synthesized in this study have a pure chalcopyrite crystal structure and do not contain byproducts such as Cu$_x$Se and In$_x$Se, which can be easily formed during the synthesis of CuInSe$_2$.[67,68]

To investigate the atomic arrangement in CISe QDs, we conducted X-ray absorption fine structure (EXAFS) analysis. When the In/Cu ratio changes for In-rich QDs, we can expect two different changes in the atomic arrangement in the crystal lattice (Figure 2D). First, Cu vacancies (V_{Cu}) are formed in the crystal (case i). Second, excessive In atoms occupy the interstitial sites (In$_i$) or anti-sites (In$_{Cu}$) (case ii). Irrespective of the In/Cu ratio, all QDs show similar k^2-weighted Cu K-edge and In K-edge EXFAS oscillations (Figure 2E,F). The Cu K-edge and In K-edge EXAFS oscillations and their Fourier-transformed (FT) spectra are well fitted with the bulk α-CuInSe$_2$ (Figure 2G,H), implying that the local environment of the Cu atoms (and In atoms) in the QDs is similar to that of the bulk chalcopyrite structure. A prominent peak in the Cu K-edge and In K-edge FT spectra of the QDs corresponds to the first-neighboring shell of Se atoms from the Cu atoms and In atoms, respectively.

If the excessive In atoms form interstitial (In$_i$) or anti-site defects (In$_{Cu}$) (case ii), additional peaks corresponding to In–In$_i$ and Cu–In$_i$ (from In$_i$), or In$_{Cu}$–Se (from In$_{Cu}$) would appear near the first neighboring shell in the In K-edge and Cu K-edge FT spectra. However, the present experimental FT spectra show a sole peak of tetrahedral In–Se or Cu–Se (Figure 2G,H). In contrast, the Cu vacancies (case i) would not affect the first neighboring shell of Se atoms from the In atoms (or Cu atoms), and the local atomic structure of In atoms (or Cu atoms) is retained regardless of the stoichiometry. This assumption (i.e., case i) is consistent with the present experimental EXAFS results. Bond lengths estimated by curve fitting with an ideal chalcopyrite structure show no

significant change as a function of the In/Cu ratio (Tables S2 and S3), suggesting that the local environment of each cation is similar regardless of the stoichiometry. Thus, the formation of interstitial (In$_i$) or anti-site defects (In$_{Cu}$) is negligible in these QDs, and the stoichiometry of the QDs is controlled by the formation of Cu vacancies.

3.3 | Optical and electrical properties of defect-engineered CISe QDs

We investigated the optical properties and band alignment of CISe QDs with a controlled amount of Cu vacancies. Figure 3A shows the absorption spectra of CISe 1–5 dispersed in dichloromethane. All absorption spectra have similar features in the visible and near-infrared range (with optical band gap energy, E_g = ~1.35 eV), regardless of the In/Cu ratio, which is favorable for solar-energy conversion because the materials can compensate for the narrow absorption range of TiO$_2$ by taking advantage of a wider region of the solar spectrum (Figure S4). Figure 3B shows the band alignment of the as-prepared CISe QDs with different Cu-vacancy densities obtained by combining cyclic voltammetry (CV) and absorption spectra results. The conduction band minimum (CBM) of the CISe QDs was determined by the first reduction peak position of the CV plots (Figure S5). The details are summarized in Table S4. Independent of the stoichiometry of CISe QDs, the energy level of CISe 1–5 was located between those of CuInSe$_2$ and CuIn$_3$Se$_5$. The position of their CBM is almost similar (-4.29 eV$_{vacuum}$) and appropriate for photogenerated carrier separation and electron transfer from the CISe QDs to TiO$_2$ (CBM = -4.33 eV$_{vacuum}$).[69] To gain insight into the photoexcited carrier dynamics in CISe QDs with various Cu-vacancy densities, time-resolved photoluminescence (TRPL) spectra were obtained from CISe QDs in dichloromethane (Figure 3C and Supporting Methods 1.1). The photoluminescence (PL) lifetime consists of three main parts: the short lifetime (τ_1) (related to the nonradiative recombination process), moderate lifetime (τ_2) (related to carrier transitions with intragap states), and long lifetime (τ_3) (related to the recombination process with donor–acceptor states) (Table S5). The fitting coefficient of the short lifetime (a_1) value is related to surface traps, and first decreases (from CISe 1 to CISe 3) and then increases (from CISe 3 to CISe 5) with increasing Cu-vacancy density. In addition, it was observed that CISe 3 (In/Cu = 1.55) has the longest average carrier lifetime (τ_{avg}) among the synthesized CISe QDs, indicating the highest probability of electron transfer from the CISe QDs to TiO$_2$.
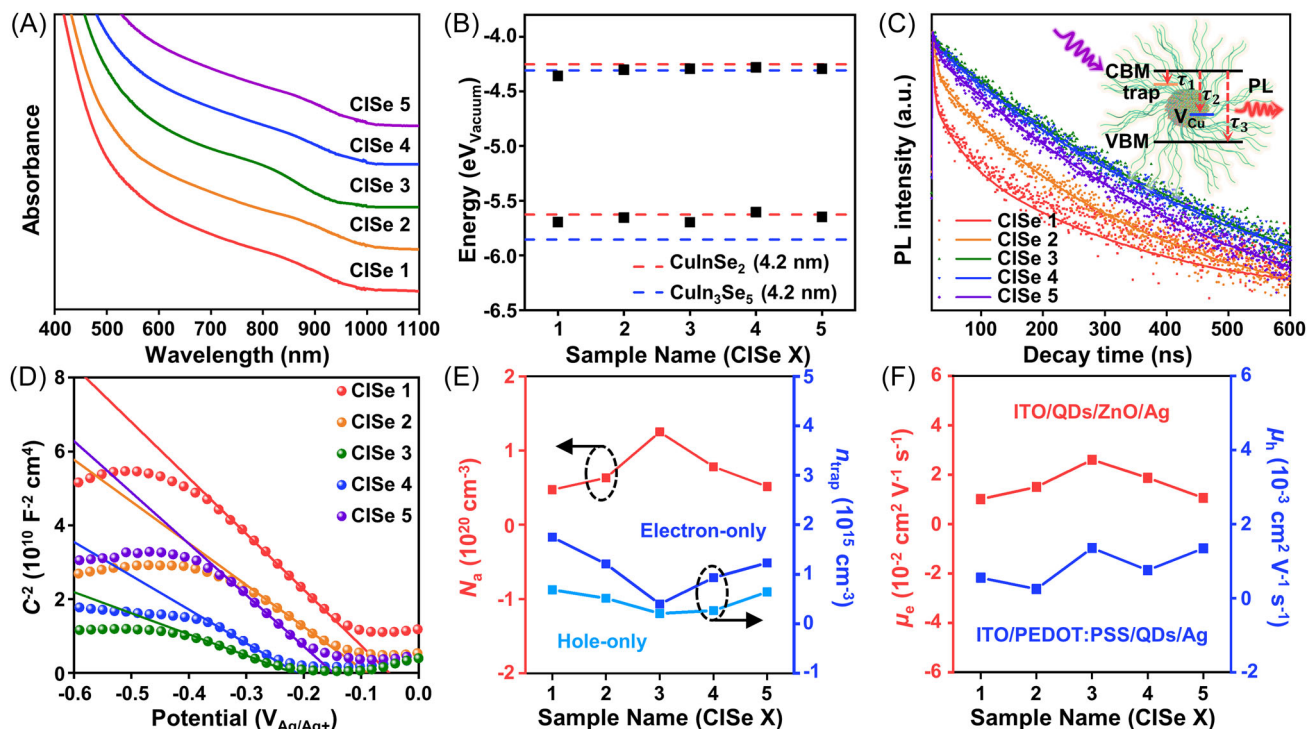
FIGURE 3 Optical and electrical properties of defect-engineered CISe QDs. (A) Absorption spectra of CISe 1–5. (B) Band alignment of CISe 1–5 determined by cyclic voltammetry and absorption spectra. Dashed blue and red lines show the calculated energy band levels of $CuInSe_2$ and $CuIn_3Se_5$ with a size of 4.2 nm, respectively. (C) Time-resolved photoluminescence (TRPL) curves of CISe 1–5 in toluene (excited at 371 nm). Inset: schematic of the PL emission mechanism of CISe QDs. (D) Mott–Schottky curves of CISe 1–5. (E) Acceptor concentration (N_a) and trap density (n_{trap}) of CISe 1–5. The acceptor concentration was determined from the Mott–Schottky curves, while the trap density was calculated from the space charge limited current (SCLC) plots of the electron- and hole-only devices. (F) Electron mobility (μ_e) and hole mobility (μ_h) of CISe 1–5, as derived from SCLC curves. Electron mobility was evaluated from the electron-only devices with an architecture of ITO/CISe QDs/ZnO/Ag, while the hole mobility was determined from the hole-only devices with a structure of ITO/PEDOT: PSS/CISe QDs/Ag.

To assess how the Cu vacancies affect the electrical properties of CISe QDs, Mott–Schottky (M–S) analysis was performed for the CISe QDs with various In/Cu ratios under dark conditions (Supporting Methods 1.1). As shown in Figure 3D and Table S6, the M–S plots of all samples have negative slopes, corresponding to typical *p*-type semiconductors with holes as the major charge carriers. The calculated acceptor concentration (N_a) values for CISe 1, 2, 3, 4, and 5 are 4.73×10^{19}, 6.32×10^{19}, 1.25×10^{20}, 7.82×10^{19}, and $5.14 \times 10^{19} \, cm^{-3}$, respectively. This is consistent with the fact that, in the bulk CISe film, the carrier concentration (N) is tuned by the densities of Cu vacancies[70,71]; a small concentration of Cu vacancies can generate free holes.[72,73]

To further elucidate the charge transport characteristics of the CISe QDs in the QD–semiconductor system, we fabricated electron- and hole-only devices with defect-engineered CISe QDs and evaluated the trap density (n_{trap}) and carrier mobility (μ) using the

space charge limited current (SCLC) method obtained from their dark current density–voltage (J_D–V) curves (Supporting Methods 1.1), as shown in Figures S6 and S7. The electron-only device consists of indium tin oxide (ITO)/CISe QDs (104 nm)/zinc oxide (ZnO, 25 nm)/silver (Ag, 90 nm), while the hole-only device consists of ITO/poly(3,4-ethylenedioxythiophene)-poly(styrenesulfonate) (PEDOT: PSS, 30 nm)/CISe QDs (104 nm)/Ag (90 nm). The resulting trap density and carrier mobility are shown in Figure 3E,F and listed in Table S7. The SCLC curves show three different parts: the linear ohmic response, the fast trap-filled region, and the quadratic child phase. Because all of the devices had the same relative dielectric constant of the semiconductor (ε), vacuum permittivity (ε_0), elementary charge (e), and film thickness of the QD (L) values, the trap density is determined by trap-field limit voltage (V_{TFL}), the intersection voltage between the ohmic and trap-filled regions of the curve. For both the electron- and

hole-only devices, the trap density is minimized for CISe 3 (Figure 3E). This is also consistent with the longer carrier lifetime of CISe 3, observed in TRPL. The carrier mobility (μ) of the CISe QDs can be assessed in the quadratic child phase. Both electron mobilities (μ_e) of the electron-only devices and hole mobilities (μ_h) of the corresponding hole-only are maximum for CISe 3. The superior charge carrier-transport capability of CISe 3 is mainly attributed to the presence of fewer traps and increased carrier concentration. These results indicate that a low trap density and high carrier mobility can be obtained by optimizing the Cu-vacancy density.

3.4 | PEC properties of CISe QDs/TiO$_2$ photoanodes

The prepared defect-engineered CISe QDs were used for PEC hydrogen production, and the influence of the Cu-vacancy density (which controls their optical and electronic properties) on the PEC performance was examined. CISe QDs were used to sensitize mesoporous TiO$_2$ films for use as photoanodes for PEC hydrogen production (Figure 4A and Section 2). The conformal and uniform coating of the CISe QDs was confirmed by scanning electron microscopy and elemental analysis (Figure S8). CISe QDs/TiO$_2$ films with ZnS passivation
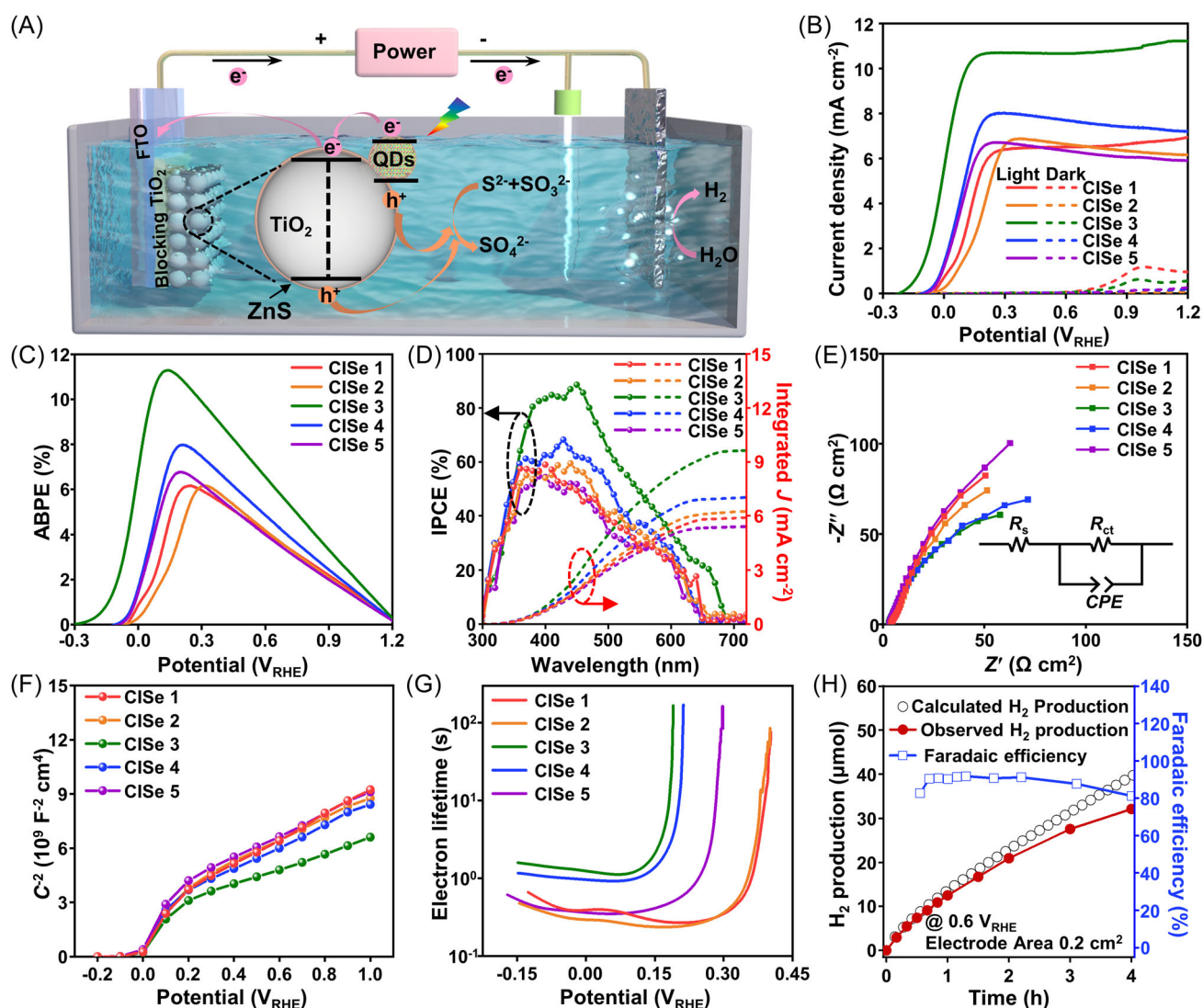

FIGURE 4 PEC hydrogen generation using photoanodes with defect-engineered CISe QDs. (A) Schematic of the PEC hydrogen evolution reaction using a CISe QDs/TiO$_2$ photoanode. (B) J–V curves, (C) ABPE curves, (D) IPCE spectra and integrated current density measured at 0.6 V$_{RHE}$, and (E) Nyquist plots of the photoanodes measured at 0.6 V$_{RHE}$ under AM 1.5 G illumination. The inset shows the equivalent circuit model used for fitting the impedance spectra. (F) Mott–Schottky plots and (G) electron lifetimes as a function of V_{OC} measured from the OCVD curves. (H) Hydrogen production over time measured at 0.6 V$_{RHE}$ for 4 h, calculated theoretical hydrogen yield, and calculated faradaic efficiency of the CISe 3/TiO$_2$ photoanode.

TABLE 2 Summary of J_{ph} of CISe QDs/TiO$_2$ photoanodes (at 0.6 V$_{RHE}$) with various In/Cu ratios.

Samples	J_{ph} (mA cm^{-2})
CISe 1	6.3 ± 0.2
CISe 2	6.4 ± 0.2
CISe 3	10.4 ± 0.3
CISe 4	7.7 ± 0.1
CISe 5	6.3 ± 0.4
Champion cell (CISe 3)	10.7

Note: For the statistical data (i.e., average and standard deviation), $n = 5$ for CISe 3 and $n = 3$ for the other samples.
Abbreviations: CISe, Cu–In–Se; QD, quantum dot.

layers were used as photoanodes, and hydrogen was generated in the platinum (Pt) cathode compartment.

Figure 4B compares the representative J–V curves of the photoanodes with various In/Cu ratios, which were obtained under both dark and light conditions. Additional J–V curves for photoanodes using CISe QDs with various compositions are shown in Figure S9 and the results are summarized in Tables 2 and S8, confirming the excellent reproducibility of our experiments. The photoanodes using CISe 1, 2, 3, 4, and 5 generated average photocurrent density (J_{ph}) values of 6.3, 6.4, 10.4, 7.7, and 6.3 mA cm^{-2} at 0.6 V$_{RHE}$, respectively, and the champion cell using CISe 3 showed a high J_{ph} of 10.7 mA cm^{-2} (0.6 V$_{RHE}$). The trend in J_{ph} as a function of the Cu-vacancy density agrees well with the trends in the electronic and optical properties discussed above. CISe 3 QDs, which have the highest N_a and carrier mobility with the lowest trap density, have a particularly high J_{ph}, which is superior to (or comparable with) most of the reported photoanodes using heavy-metal-free QDs (Table S9).

Photoanodes without QD sensitization showed low photocurrent density (Figure S10), demonstrating that the majority of photo-excited charge carriers were produced by QDs. In addition, PEC performance without sacrificial agents was very low (Figure S11), because the valence band position of CISe QDs is comparable with the water oxidation potential, resulting in poor hole transfer from QDs. The photoanode without QDs (TiO$_2$/ZnS) showed J_{ph} of 0.69 mA cm^{-2} at 0.6 V$_{RHE}$, which was very similar to that of the photoanode with QDs (0.67 mA cm^{-2} at 0.6 V$_{RHE}$). This suggests that the contribution from CISe QDs is negligible in the absence of sacrificial agents. Furthermore, typically, in the sacrificial-agent-free system, metal chalcogenide QDs show much lower PEC performances and suffer significant photocorrosion, primarily due to slower transfer of

photogenerated holes. Therefore, there have been only a few studies investigating the overall water-splitting performances of metal chalcogenide QDs in the absence of sacrificial agents, which have reported low J_{ph} values (0.2–2.0 mA cm^{-2} at 0.6 V$_{RHE}$) using QDs such as CdSe, CdTe, or CdS.[28,74–76]

Figure 4C shows the corresponding applied bias photon-to-current efficiency (ABPE) curves from J–V curves (Supporting Methods 1.2). CISe 3 shows the highest J_{ph} and ABPE, as well as the most negative onset potential. The outstanding PEC performances of photoanodes using CISe 3 can be attributed to several synergistic effects: (1) appropriate electronic energy levels accelerate electron transfer from QDs to TiO$_2$ and suppress photogenerated electron–hole recombination and (2) high carrier concentration and fast carrier mobility in CISe 3 increase the chance of electron transfer. In addition, the lower trap density can minimize the nonradiative recombination associated with QDs and reduce interfacial electron recombination with the electrolyte.[64,77]

Figure 4D shows the incident photon-to-current conversion efficiency (IPCE) spectra and integrated current density measured at 0.6 V$_{RHE}$ as a function of the In/Cu ratios of the CISe QDs. The trend in the integrated current density from the IPCE agrees well with that of the J_{ph} values obtained from the J–V curves due to the similar spectral absorption range of all QDs. The highest IPCE values over the entire spectral range are obtained for photoanodes with CISe 3. This is attributed to the higher electron injection and collection efficiencies[78] in this photoanode compared with the other samples, considering the similar optical E_g of all QDs.

To better understand the relationship between the electronic properties of the QDs and the resulting PEC properties, EIS analysis was performed using the CISe QDs/TiO$_2$ photoanodes (Supporting Methods 1.2). Figure 4E shows Nyquist plots of the CISe QDs/TiO$_2$ photoanodes with various In/Cu ratios. The equivalent circuit model is shown in the inset of Figure 4E, which contains a series resistance (R_s) and an RC circuit representing the charge-transfer properties at the interface between the photoanodes and redox couples in the electrolyte.[47,79] In particular, the interfacial charge-transfer resistance (R_{ct}) in the RC circuit is related to the charge-transfer rate at the photoanode–electrolyte interface. The fitting parameter R_{ct} decreases in the order of CISe 5 > 1 > 2 > 4 > 3 (Table S10). This order is the same as that for the impedance data obtained under dark conditions (Figure S12). Based on the TRPL results and the trends in the electronic properties, it can be concluded that the QDs with higher carrier lifetime and carrier mobility show more efficient charge

separation and hole transfer to the redox couples in the electrolyte, leading to superior PEC performance.[80]

To estimate the carrier concentration (N) and flat-band potential (V_{FB}) of each photoanode, M–S analysis was performed (Figure 4F). All photoanodes yielded M–S plots with a positive slope, which is attributed to the *n*-type behavior of TiO_2. The evaluated donor concentration (N_d) and V_{FB} values for CISe QDs/TiO_2 photoanodes with various In/Cu ratios are listed in Table S11. Photoanodes with CISe 3 have the highest N_d and the most negative V_{FB} among the five QDs, indicating more efficient charge separation and transport of the photogenerated electrons[81–85] compared to the other samples. These observations are attributed to reduced nonradiative recombination, and interfacial electron recombination with the electrolyte for the photoanodes with CISe 3, which is in good agreement with the results of the *J–V* curves and EIS analysis discussed earlier.

The electron lifetime (τ_e) value in each photoanode was evaluated using the open-circuit voltage decay (OCVD) method (Supporting Methods 1.2), and the decay of open-circuit voltage (V_{OC}) caused by electron recombination at the photoanode–electrolyte interface after stationary illumination (AM 1.5 G condition) was abruptly switched off (Figure S13). The highest τ_e value was obtained for photoanodes with CISe 3 among the photoanodes with 5 different CISe QDs (Figure 4G). Because the surface traps of QDs are one of the major pathways for interfacial electron recombination between the photoanode and the oxidized form of the redox couple,[77,86] it can be presumed that QDs with a lower trap density have slower interfacial electron recombination with the electrolyte, leading to a longer τ_e in the photoanode. In summary, the *J–V* curves, EIS data, M–S plots, and OCVD curves all indicated the same trend; that is, the higher carrier mobility and lower trap density of CISe QDs lead to more efficient charge separation and transport in the photoanodes with CISe 3, eventually resulting in superior PEC hydrogen production performance.

The actual hydrogen production was tested for CISe $3/TiO_2$ photoanodes at 0.6 V_{RHE} for 4 h, and hydrogen was collected in the headspace of the PEC reactor (Section 2). The evolved hydrogen was quantified by GC during the reaction (Figures 4H and S14). The Faradaic efficiency was retained at ~90%, suggesting that most of the current measured during the PEC reaction induces hydrogen production. A degraded Faradaic efficiency was expected because it is difficult to account for all of the produced gas; some of the evolved gas can be trapped on the electrode or dissolved in the electrolyte.[28] In addition, corrosion of QDs can occur, caused by the accumulation of photogenerated holes on the QDs during

the 4 h chronoamperometry test, which contributes to measurement uncertainties to some degree.[87]

The degradation process was examined by XRD and XPS analyses on the photoanodes working for 0 min, 10 min, 2 h, and 4 h of the chronoamperometry test (Figure S15). There was no significant shift in the position of the (112) peak of CISe in the XRD pattern, which confirms that the crystal structures of QDs were maintained. All XPS peaks were observed to shift towards higher binding energies with increasing test time, and the intensity of the oxidized S peaks increased significantly, which can be assigned to the partial surface oxidation of CISe QDs and ZnS layers.[88] Consequently, the stability of photoanodes can be further enhanced by the introduction of additional passivation layers.[65] For example, CISe $3/TiO_2$ photoanodes with ZnS/SiO_2 passivation layers showed improved stability (Figure S14; see Figure S16 for their *J–V* and ABPE curves and the Experimental Section for the SiO_2 passivation method). The result is comparable to previous studies using heavy-metal-free QDs (Table S9), although further improvements are required to match those using Cd-based QDs (e.g., maintaining 83% of its initial value after four hours in a representative previous work).[88] From the results, it was clear that the total amount of hydrogen generation increased (Figure S17), despite the slightly lower J_{ph} at 0.6 V_{RHE} (9.9 mA cm^{-2} on average for $n = 3$, Figure S16A).

Surprisingly, the same trends were observed for QDSCs fabricated based on CISe QDs/TiO_2 photoanodes (Supporting Methods 1.3 and Figure S18). The resulting photovoltaic parameters are summarized in Figure S19 and Table S12. QDSCs with CISe 3 show the highest short-circuit current density (J_{SC}) and conversion efficiency (η). The influence of the Cu-vacancy density on the interfacial electron recombination and τ_e in the photoanodes of QDSCs was examined using EIS (Figure S20).[89] The inset of Figure S20A shows the equivalent circuit model used to fit the EIS curves of the QDSCs, which includes R_s, an impedance at the interface of the electrolyte/Cu_2S counter electrode (R_{CE} and CPE_1), and impedance at the electrolyte/photoanode interface (R_{ct} and CPE_2).[64,89] QDSCs with CISe 3 have the highest R_{ct} values, implying that the interfacial electron recombination between the photoanode and the electrolyte is relatively low for these QDSCs. This is attributed to the relatively low surface trap density. However, the C_μ values are almost similar to each other, indicating that the CBM potential of TiO_2 is not affected by the Cu-vacancy density of the adsorbed QDs. As a result, the τ_e values, which were determined as the product of R_{ct} and C_μ values, are higher for CISe 3 (Figure S20C), resulting in the superior photovoltaic properties of QDSCs. The

results highlight that the superior electronic properties achieved through defect engineering are advantageous for both solar-to-chemical and solar-to-electrical energy conversion.

4 | CONCLUSION

In summary, eco-friendly CISe QDs with controllable concentrations of Cu defects were prepared by a hot-injection method using various metal precursor combinations and used as light absorbers to improve the H_2 generation performance of TiO_2 photoanodes. The Lewis acid–base reaction between metal halide–oleylamine complexes and ammonium selenocarbamate was regulated considering the relative strengths of the acids, producing CISe QDs with a wide range of In/Cu ratios but a similar size and shape. XRD and EXAFS results showed that the QDs have a chalcopyrite structure with Cu vacancies, and the density of Cu vacancies can be controlled by the In/Cu ratio. The energy levels, carrier concentrations, and lifetimes of CISe QDs were tuned by modifying the Cu-vacancy density. The CISe QDs with an In/Cu ratio of 1.55 had the highest carrier concentration and longest lifetime among all QDs. Benefiting from this, a photoanode using CISe QDs with an In/Cu ratio of 1.55 achieved a high photocurrent density of 10.7 mA cm^{-2} at 0.6 V$_{RHE}$ for PEC hydrogen production. The same trends were observed for CISe QDSCs, supporting its general impact on solar-energy conversion. The improved carrier dynamics in QDs with Cu vacancies leads to efficient separation and transport of photogenerated carriers. Our study suggests that defect engineering of nontoxic ternary QDs can be systematically achieved by controlling colloidal synthesis. Although significant effort is required in future work to enhance the stability of QD-based photoanodes, the resulting QDs have significant potential as efficient solar absorbers for solar-driven optoelectronic devices.

CONFLICT OF INTEREST STATEMENT
The authors declare no conflicts of interest.

ORCID
Hwapyong Kim http://orcid.org/0000-0002-9409-8218
Jiwoong Yang http://orcid.org/0000-0002-2346-8197

REFERENCES

1. Fujishima A, Honda K. Electrochemical photolysis of water at a semiconductor electrode. *Nature.* 1972;238(5358):37-38.
2. Wang L, Si W, Tong Y, et al. Graphitic carbon nitride (*g*-C$_3$N$_4$)-based nanosized heteroarrays: promising materials for photo-electrochemical water splitting. *Carbon Energy.* 2020;2(2):223-250.
3. Pan S, Li J, Wen Z, et al. Halide perovskite materials for photo (electro) chemical applications: dimensionality, heterojunction, and performance. *Adv Energy Mater.* 2022;12(4):2004002.
4. Velásquez DAP, Sousa FLN, Soares TAS, et al. Boosting the performance of TiO$_2$ nanotubes with ecofriendly AgIn$_5$Se$_8$ quantum dots for photoelectrochemical hydrogen generation. *J Power Sources.* 2021;506:230165.
5. Luo B, Liu J, Guo H, et al. High efficiency photoelectrochemical hydrogen generation using eco-friendly Cu doped Zn-In-Se colloidal quantum dots. *Nano Energy.* 2021;88:106220.
6. Guo H, Liu J, Luo B, et al. Unlocking the effects of Cu doping in heavy-metal-free AgIn$_5$S$_8$ quantum dots for highly efficient photoelectrochemical solar energy conversion. *J Mater Chem C.* 2021;9(30):9610-9618.
7. Wahl S, El-Refaei SM, Buzanich AG, et al. Zn$_{0.35}$Co$_{0.65}$O—A stable and highly active oxygen evolution catalyst formed by zinc leaching and tetrahedral coordinated cobalt in wurtzite structure. *Adv Energy Mater.* 2019;9(20):1900328.
8. Han H, Bai Z, Zhang T, et al. Hierarchical design and development of nanostructured trifunctional catalysts for electrochemical oxygen and hydrogen reactions. *Nano Energy.* 2019;56:724-732.
9. Ramalingam V, Varadhan P, Fu HC, et al. Heteroatom-mediated interactions between ruthenium single atoms and an MXene support for efficient hydrogen evolution. *Adv Mater.* 2019;31(48):1903841.
10. Geng S, Tian F, Li M, et al. Activating interfacial S sites of MoS$_2$ boosts hydrogen evolution electrocatalysis. *Nano Res.* 2022;15(3):1809-1816.
11. Kale VS, Sim U, Yang J, et al. Sulfur-modified graphitic carbon nitride nanostructures as an efficient electrocatalyst for water oxidation. *Small.* 2017;13(17):1603893.
12. Unnarkat AP, Sridhar T, Wang H, Mahajani SM, Suresh AK. Study of cobalt molybdenum oxide supported on mesoporous silica for liquid phase cyclohexane oxidation. *Catal Today.* 2018;310:116-129.
13. Fan Z, Luo Z, Huang X, et al. Synthesis of 4H/*fcc* noble multimetallic nanoribbons for electrocatalytic hydrogen evolution reaction. *J Am Chem Soc.* 2016;138(4):1414-1419.
14. Nsanzimana JMV, Peng Y, Miao M, et al. An earth-abundant tungsten–nickel alloy electrocatalyst for superior hydrogen evolution. *ACS Appl Nano Mater.* 2018;1(3):1228-1235.
15. Zhang L, Ye X, Boloor M, Poletayev A, Melosh NA, Chueh WC. Significantly enhanced photocurrent for water oxidation in monolithic Mo:BiVO$_4$/SnO$_2$/Si by thermally increasing the minority carrier diffusion length. *Energy Environ Sci.* 2016;9(6):2044-2052.
16. Shi X, Choi IY, Zhang K, et al. Efficient photoelectrochemical hydrogen production from bismuth vanadate-decorated tungsten trioxide helix nanostructures. *Nat Commun.* 2014;5:4775.
17. Pan Q, Li A, Zhang Y, Yang Y, Cheng C. Rational design of 3D hierarchical ternary SnO$_2$/TiO$_2$/BiVO$_4$ arrays photoanode

toward efficient photoelectrochemical performance. *Adv Sci.* 2019;7(3):1902235.

18. Kim S, Cho Y, Rhee R, Park JH. Black TiO_2: what are exact functions of disorder layer. *Carbon Energy.* 2020;2(1):44-53.

19. Franz S, Arab H, Chiarello GL, Bestetti M, Selli E. Single-step preparation of large area TiO_2 photoelectrodes for water splitting. *Adv Energy Mater.* 2020;10(23):2000652.

20. Yang Y, Jin Q, Mao D, et al. Dually ordered porous TiO_2-rGO composites with controllable light absorption properties for efficient solar energy conversion. *Adv Mater.* 2017;29(4):1604795.

21. Han X, Wu X, Deng Y, et al. Ultrafine Pt nanoparticle-decorated pyrite-type CoS_2 nanosheet arrays coated on carbon cloth as a bifunctional electrode for overall water splitting. *Adv Energy Mater.* 2018;8(24):1800935.

22. Shen C, Wierzbicka E, Schultz T, Wang R, Koch N, Pinna N. Atomic layer deposition of MoS_2 decorated TiO_2 nanotubes for photoelectrochemical water splitting. *Adv Mater Interfaces.* 2022;9(20):2200643.

23. Li J, Yuan H, Zhang W, et al. Advances in Z-scheme semiconductor photocatalysts for the photoelectrochemical applications: a review. *Carbon Energy.* 2022;4(3):294-331.

24. Huang H, Zhao J, Du Y, et al. Direct Z-scheme heterojunction of semicoherent $FAPbBr_3$/Bi_2WO_6 interface for photoredox reaction with large driving force. *ACS Nano.* 2020;14(12):16689-16697.

25. Yuan YJ, Chen DQ, Xiong M, et al. Bandgap engineering of $(AgIn)_xZn_{2(1-x)}S_2$ quantum dot photosensitizers for photocatalytic H_2 generation. *Appl Catal B.* 2017;204:58-66.

26. Pandey A, Guyot-Sionnest P. Slow electron cooling in colloidal quantum dots. *Science.* 2008;322(5903):929-932.

27. Ren S, Wang M, Wang X, et al. Near-infrared heavy-metal-free SnSe/ZnSe quantum dots for efficient photoelectrochemical hydrogen generation. *Nanoscale.* 2021;13(6):3519-3527.

28. Kim JY, Jang YJ, Park J, et al. Highly loaded PbS/Mn-doped CdS quantum dots for dual application in solar-to-electrical and solar-to-chemical energy conversion. *Appl Catal B.* 2018;227(8):409-417.

29. Abdelkarim O, Mirzaei A, Selopal GS, et al. Constructing quantum dots sensitized TiO_2 nanotube p-n heterojunction for photoelectrochemical hydrogen generation. *Chem Eng J.* 2022;446:137312.

30. Ghorpade UV, Suryawanshi MP, Shin SW, et al. Unassisted visible solar water splitting with efficient photoelectrodes sensitized by quantum dots synthesized via an environmentally friendly eutectic solvent-mediated approach. *J Mater Chem A.* 2018;6(45):22566-22579.

31. Zhao H, Liu G, Vidal F, Wang Y, Vomiero A. Colloidal thick-shell pyramidal quantum dots for efficient hydrogen production. *Nano Energy.* 2018;53:116-124.

32. Wang Z, Zhu H, Tu W, et al. Host/guest nanostructured photoanodes integrated with targeted enhancement strategies for photoelectrochemical water splitting. *Adv Sci.* 2022;9(2):2103744.

33. Ding C, Liu F, Zhang Y, et al. Photoexcited hot and cold electron and hole dynamics at $FAPbI_3$ perovskite quantum dots/metal oxide heterojunctions used for stable perovskite quantum dot solar cells. *Nano Energy.* 2020;67:104267.

34. Li Y, Zhu J, Huang Y, et al. Efficient inorganic solid solar cells composed of perovskite and PbS quantum dots. *Nanoscale.* 2015;7(21):9902-9907.

35. Zheng Z, Gan L, Zhang J, Zhuge F, Zhai T. An enhanced UV–Vis–NIR and flexible photodetector based on electrospun ZnO nanowire array/PbS quantum dots film heterostructure. *Adv Sci.* 2017;4(3):1600316.

36. Li L, Gu L, Lou Z, Fan Z, Shen G. ZnO quantum dot decorated Zn_2SnO_4 nanowire heterojunction photodetectors with drastic performance enhancement and flexible ultraviolet image sensors. *ACS Nano.* 2017;11(4):4067-4076.

37. Caruge JM, Halpert JE, Wood V, Bulović V, Bawendi MG. Colloidal quantum-dot light-emitting diodes with metal-oxide charge transport layers. *Nat Photon.* 2008;2(4):247-250.

38. Liu Z, Lin CH, Hyun BR, et al. Micro-light-emitting diodes with quantum dots in display technology. *Light Sci Appl.* 2020;9(1):83.

39. Selopal GS, Abdelkarim O, Kumar P, et al. Role of interfacial engineering of "giant" core–shell quantum dots. *ACS Appl Energy Mater.* 2022;5(2):1447-1459.

40. Huang J, Gatty MG, Xu B, et al. Covalently linking $CuInS_2$ quantum dots with a Re catalyst by click reaction for photocatalytic CO_2 reduction. *Dalton Trans.* 2018;47(31):10775-10783.

41. Wu L, Chen SY, Fan FJ, Zhuang TT, Dai CM, Yu SH. Polytypic nanocrystals of Cu-based ternary chalcogenides: colloidal synthesis and photoelectrochemical properties. *J Am Chem Soc.* 2016;138(17):5576-5584.

42. Li F, Zhang M, Benetti D, et al. "Green", gradient multi-shell $CuInSe_2$/$(CuInSe_xS_{1-x})_5$/$CuInS_2$ quantum dots for photoelectrochemical hydrogen generation. *Appl Catal B.* 2021;280:119402.

43. Wang R, Tong X, Channa AI, et al. Environmentally friendly Mn-alloyed core/shell quantum dots for high-efficiency photoelectrochemical cells. *J Mater Chem A.* 2020;8(21):10736-10741.

44. Zhao H, Zhang H, Liu G, et al. Ultra-small colloidal heavy-metal-free nanoplatelets for efficient hydrogen generation. *Appl Catal B.* 2019;250:234-241.

45. Tong X, Zhou Y, Jin L, et al. Heavy metal-free, near-infrared colloidal quantum dots for efficient photoelectrochemical hydrogen generation. *Nano Energy.* 2017;31:441-449.

46. You Y, Tong X, Channa AI, et al. Tailoring the optoelectronic properties of eco-friendly $CuGaS_2$/ZnSe core/shell quantum dots for boosted photoelectrochemical solar hydrogen production. *EcoMat.* 2022;4(5):e12206.

47. Kim J, Jang YJ, Baek W, et al. Highly efficient photoelectrochemical hydrogen production using nontoxic $CuIn_{1.5}Se_3$ quantum dots with ZnS/SiO_2 double overlayers. *ACS Appl Mater Interfaces.* 2022;14(1):603-610.

48. Long Z, Tong X, Wang R, et al. Engineered environment-friendly colloidal core/shell quantum dots for high-efficiency solar-driven photoelectrochemical hydrogen evolution. *ChemSusChem.* 2022;15(10):e202200346.

49. Bai S, Zhang N, Gao C, Xiong Y. Defect engineering in photocatalytic materials. *Nano Energy.* 2018;53:296-336.

50. Adamczyk JM, Gomes LC, Qu J, et al. Native defect engineering in $CuInTe_2$. *Chem Mater.* 2021;33(1):359-369.

51. Guo Y, Li H, Ma W, Shi W, Zhu Y, Choi W. Photocatalytic activity enhanced via surface hybridization. *Carbon Energy*. 2020;2(3):308-349.

52. Xia C, Surendran S, Ji S, et al. A sulfur self-doped multifunctional biochar catalyst for overall water splitting and a supercapacitor from *Camellia japonica* flowers. *Carbon Energy*. 2022;4(4):491-505.

53. Rincón C, Márquez R. Defect physics of the CuInSe$_2$ chalcopyrite semiconductor. *J Phys Chem Solids*. 1999;60(11):1865-1873.

54. Saniz R, Bekaert J, Partoens B, Lamoen D. Structural and electronic properties of defects at grain boundaries in CuInSe$_2$. *Phys Chem Chem Phys*. 2017;19(22):14770-14780.

55. Draguta S, McDaniel H, Klimov VI. Tuning carrier mobilities and polarity of charge transport in films of CuInSe$_x$S$_{2-x}$ quantum dots. *Adv Mater*. 2015;27(10):1701-1705.

56. Duncan TV, Bajaj A, Gray PJ. Surface defects and particle size determine transport of CdSe quantum dots out of plastics and into the environment. *J Hazard Mater*. 2022;439:129687.

57. Chen YC, Chang HH, Hsu YK. Synthesis of CuInS$_2$ quantum dots/In$_2$S$_3$/ZnO nanowire arrays with high photoelectrochemical activity. *ACS Sustainable Chem Eng*. 2018;6(8):10861-10868.

58. Orfield NJ, McBride JR, Keene JD, Davis LM, Rosenthal SJ. Correlation of atomic structure and photoluminescence of the same quantum dot: pinpointing surface and internal defects that inhibit photoluminescence. *ACS Nano*. 2015;9(1):831-839.

59. Zang H, Li H, Makarov NS, et al. Thick-shell CuInS$_2$/ZnS quantum dots with suppressed "blinking" and narrow single-particle emission line widths. *Nano Lett*. 2017;17(3):1787-1795.

60. Yang J, Kim JY, Yu JH, et al. Copper–indium–selenide quantum dot-sensitized solar cells. *Phys Chem Chem Phys*. 2013;15(47):20517-20525.

61. Panthani MG, Stolle CJ, Reid DK, et al. CuInSe$_2$ quantum dot solar cells with high open-circuit voltage. *J Phys Chem Lett*. 2013;4(12):2030-2034.

62. Son JS, Wen XD, Joo J, et al. Large-scale soft colloidal template synthesis of 1.4 nm thick CdSe nanosheets. *Angew Chem Int Ed*. 2009;48(37):6861-6864.

63. Yu JH, Kim J, Hyeon T, Yang J. Facile synthesis of manganese (II)-doped ZnSe nanocrystals with controlled dimensionality. *J Chem Phys*. 2019;151(24):244701.

64. Kim JY, Yang J, Yu JH, et al. Highly efficient copper–indium–selenide quantum dot solar cells: suppression of carrier recombination by controlled ZnS overlayers. *ACS Nano*. 2015;9(11):11286-11295.

65. Zhao K, Pan Z, Mora-Seró I, et al. Boosting power conversion efficiencies of quantum-dot-sensitized solar cells beyond 8% by recombination control. *J Am Chem Soc*. 2015;137(16):5602-5609.

66. Paszkowicz W, Lewandowska R, Bacewicz R. Rietveld refinement for CuInSe$_2$ and CuIn$_3$Se$_5$. *J Alloys Compd*. 2004;362(1-2):241-247.

67. Kuznetsov MV, Shalaeva EV, Yakushev MV, Tomlinson RD. Evolution of CuInSe$_2$ (1 1 2) surface due to annealing: XPS study. *Surf Sci*. 2003;530(1-2):L297-L301.

68. Kim JS, Baek SK, Kim YB, et al. Copper indium selenide water splitting photoanodes with artificially designed heterophasic blended structure and their high photoelectrochemical performances. *Nano Energy*. 2018;46:1-10.

69. Butler MA, Ginley DS. Prediction of flatband potentials at semiconductor–electrolyte interfaces from atomic electronegativities. *J Electrochem Soc*. 1978;125(2):228-232.

70. Wang Z, Zhang L, Schülli TU, et al. Identifying copper vacancies and their role in the CuO based photocathode for water splitting. *Angew Chem Int Ed*. 2019;58(49):17604-17609.

71. Bertoni G, Ramasse Q, Brescia R, De Trizio L, De Donato F, Manna L. Direct quantification of Cu vacancies and spatial localization of surface plasmon resonances in copper phosphide nanocrystals. *ACS Mater Lett*. 2019;1(6):665-670.

72. Bekenstein Y, Vinokurov K, Keren-Zur S, et al. Thermal doping by vacancy formation in copper sulfide nanocrystal arrays. *Nano Lett*. 2014;14(3):1349-1353.

73. Rettie AJE, Sturza M, Malliakas CD, Botana AS, Chung DY, Kanatzidis MG. Copper vacancies and heavy holes in the two-dimensional semiconductor KCu$_{3-x}$Se$_2$. *Chem Mater*. 2017;29(14):6114-6121.

74. Chen HM, Chen CK, Chang YC, et al. Quantum dot monolayer sensitized ZnO nanowire-array photoelectrodes: true efficiency for water splitting. *Angew Chem*. 2010;122(34):6102-6105.

75. Miao J, Yang HB, Khoo SY, Liu B. Electrochemical fabrication of ZnO–CdSe core–shell nanorod arrays for efficient photoelectrochemical water splitting. *Nanoscale*. 2013;5(22):11118-11124.

76. Yin H, Yi J, Yang ZW, et al. Plasmon enhanced quantum dots fluorescence and energy conversion in water splitting using shell-isolated nanoparticles. *Nano Energy*. 2017;42:232-240.

77. Kamat PV. Quantum dot solar cells. the next big thing in photovoltaics. *J Phys Chem Lett*. 2013;4(6):908-918.

78. Kelkar S, Ballal C, Deshpande A, Warule S, Ogale S. Quantum dot CdS coupled Cd$_2$SnO$_4$ photoanode with high photoelectrochemical water splitting efficiency. *J Mater Chem A*. 2013;1(40):12426-12431.

79. Zhou S, Cai Y, Zhang J, Liu Y, Zhou L, Lei J. Au-loaded resorcinol–formaldehyde resin photocatalysts: hollow sphere structure design and localized surface plasmon resonance effect synergistically promote efficient nicotinamide adenine dinucleotide (NADH) regeneration. *ACS Sustainable Chem Eng*. 2022;10(44):14464-14473.

80. Rahman MZ, Edvinsson T, Gascon J. Hole utilization in solar hydrogen production. *Nat Rev Chem*. 2022;6(4):243-258.

81. Zhu H, Zhao M, Zhou J, et al. Surface states as electron transfer pathway enhanced charge separation in TiO$_2$ nanotube water splitting photoanodes. *Appl Catal B*. 2018;234:100-108.

82. Ling Y, Wang G, Wheeler DA, Zhang JZ, Li Y. Sn-doped hematite nanostructures for photoelectrochemical water splitting. *Nano Lett*. 2011;11(5):2119-2125.

83. Sivula K. Mott–Schottky analysis of photoelectrodes: sanity checks are needed. *ACS Energy Lett*. 2021;6(7):2549-2551.

84. Ikram A, Sahai S, Rai S, Dass S, Shrivastav R, Satsangi VR. Improved charge transportation at PbS QDs/TiO$_2$ interface for efficient PEC hydrogen generation. *Phys Chem Chem Phys*. 2016;18(23):15815-15821.

85. Subramanyam P, Meena B, Suryakala D, Subrahmanyam C. TiO_2 photoanodes sensitized with Bi_2Se_3 nanoflowers for visible–near-infrared photoelectrochemical water splitting. *ACS Appl Nano Mater.* 2021;4(1):739-745.

86. Tong X, Channa AI, You Y, et al. Boosting the performance of eco-friendly quantum dots-based photoelectrochemical cells via effective surface passivation. *Nano Energy.* 2020;76:105062.

87. Toe CY, Zheng Z, Wu H, Scott J, Amal R, Ng YH. Photocorrosion of cuprous oxide in hydrogen production: rationalising self-oxidation or self-reduction. *Angew Chem Int Ed.* 2018;57(41):13613-13617.

88. Zhang H, Besteiro LV, Liu J, et al. Efficient and stable photoelectrochemical hydrogen generation using optimized colloidal heterostructured quantum dots. *Nano Energy.* 2021;79:105416.

89. Longo C, Nogueira AF, De Paoli MA, Cachet H. Solid-state and flexible dye-sensitized TiO_2 solar cells: a study by electrochemical impedance spectroscopy. *J Phys Chem B.* 2002;106(23):5925-5930.

SUPPORTING INFORMATION

Additional supporting information can be found online in the Supporting Information section at the end of this article.